Decay dynamics of radiatively coupled quantum dots in photonic crystal slabs

Philip Trøst Kristensen,[1] Jesper Mørk,[1] Peter Lodahl,[1] and Stephen Hughes[2]
[1]*DTU Fotonik, Technical University of Denmark, DK-2800 Kgs. Lyngby, Denmark*
[2]*Department of Physics, Queen's University, Ontario, Canada K7L 3N6*
(Received 28 June 2010; revised manuscript received 11 October 2010; published 14 February 2011)

We theoretically investigate the influence of radiative coupling on light emission in a photonic crystal slab structure. The calculation method is based on a formalism that combines the photon Green's tensor with a self-consistent Dyson equation approach and is applicable to a wide range of problems in nanophotonics. We apply the method to calculate how resonant interactions of neighboring quantum dots affect the spontaneous emission, and we observe a pronounced nonexponential decay in the intensity at the detector position. We analyze the decay based on detailed calculations of the Green's tensor and show how interference between different light scattering pathways is responsible for this nontrivial detector response.

DOI: 10.1103/PhysRevB.83.075305 PACS number(s): 78.67.Hc

I. INTRODUCTION

Semiconductor quantum dots (QDs) are fascinating nanostructures that allow for confinement of carrier motion to limited regions of the host material. This leads to quantization effects in which the energy level structure can be engineered by changing the QD size and shape, and in which transitions between different energy levels may be mediated by the emission of light quanta (photons). Light emission from QDs is of great importance in applications such as lasers and single-photon sources[1,2] in future quantum information networks,[3] and is therefore of both practical and theoretical interest.

Light sources in the form of QDs may be combined with the unique dispersion properties of photonic crystals[4–6] (PCs) to control the decay rate[7–9], the propagation direction,[10–13] or even the qualitative nature[14–16] of the emitted light. PCs are periodically structured on a length scale comparable to the light wavelength, and multiple scattering from the periodic structure alters the optical properties of the material in a controlled way. QDs in a PC act not only as sources of light but inevitably lead to additional scattering. Indeed, the mere inclusion of a QD in an otherwise perfect PC will change the electromagnetic response of the system. This effect has been seen to degrade the Q-factor of micro cavities[17] and may be of importance in recent experiments with self-assembled QDs.[9] Compared to the spectral properties of most PCs, however, the linewidth of single QDs is extremely narrow ($\sim\mu$eV) which means that the QDs will act as scatterers only within a very narrow frequency interval. The relatively narrow linewidths are due to low temperature reduction of nonradiative electron-phonon scattering and a nominally long radiative decay. The radiation contribution can, in principle, be controlled by external means (e.g., by tuning the QD energy levels), and a detailed understanding of the scattering properties of QDs is thus of interest from both a fundamental point of view and for possible future applications.

Theoretically, light scattering is conveniently described in terms of the Green's tensor, $\mathbf{G}(\mathbf{r},\mathbf{r}')$, which is the classical electromagnetic propagator that includes information of all scattering channels in the structure. In particular, it contains local properties such as the local density of states[18] (LDOS). The LDOS describes the availability and field strength of electromagnetic modes at a given frequency and position, and the decay rate of a single excited QD is proportional to the LDOS. In this article we use a self-consistent Dyson equation approach to calculate the Green's tensor. This enables a transparent and physically appealing analysis of light emission and propagation that includes the additional scattering from QDs in the structure. The method is applicable to a wide range of problems in nanophotonics and has recently been used to investigate QD light emission[19] and entanglement[20] in PC cavity systems for which analytical approximations to the Green's tensors were used. In this work, we present the method in a general form and apply it using a numerically calculated Green's tensor for a photonic crystallite, as illustrated in Fig. 1. Similar structures have previously been investigated in Ref. 32 in which the LDOS was calculated at a number of positions within the Wigner-Seitz cell. Contrary to Ref. 32, we present both the local properties $\mathbf{G}(\mathbf{r},\mathbf{r})$ and the nonlocal properties $\mathbf{G}(\mathbf{r},\mathbf{r}')$ to describe the interaction of spatially separated QDs within the PC (red and green spheres in Fig. 1). A number of previous calculations on quantum dot interactions have been mainly concerned with the spectral properties[19] or internal quantum states.[20] We focus in this work on the time-domain dynamics as observed in the intensity of the emitted light. This is the quantity that is measured in time-resolved photoluminescence experiments,[9] and we show that the inclusion of additional scattering from a second QD can fundamentally change the decay dynamics from that of the one-QD case.

This article is organized as follows. In Sec. II we introduce the theoretical framework used for the modeling of nanophotonic structures with multiple QDs. The method is presented in a general form that allows for direct interpretation in terms of different possible scattering channels by which light can travel from a QD to the detector. Section III presents calculations of the Green's tensor for a finite-sized photonic crystallite in a dielectric slab and, finally, in Sec. IV, the results of Secs. II and III are combined to study spontaneous emission from two QDs in a photonic crystal slab.

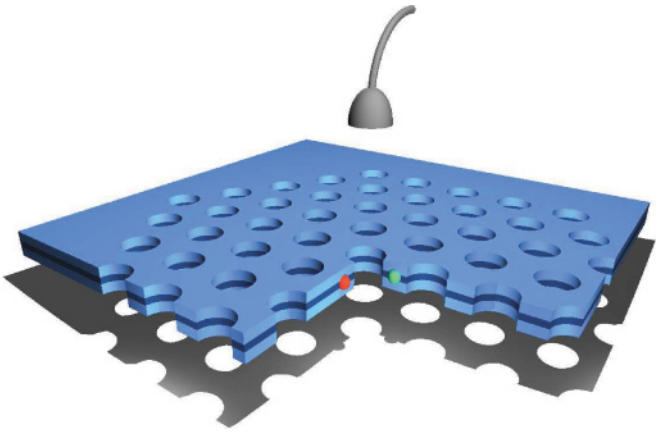

FIG. 1. (Color online) Sketch of photonic crystallite. Red and green spheres represent embedded QDs at two high-symmetry points of the central Wigner-Seitz cell and a detector is placed above the central air hole of the crystallite.

II. THEORETICAL FRAMEWORK

A. Classical light emission and propagation

We shall consider light emission and propagation in general nonmagnetic material systems described by the relative permittivity $\epsilon_r(\mathbf{r})$. In the absence of sources, the classical electric field solves the Helmholtz equation:

$$\nabla \times \nabla \times \mathbf{E}(\mathbf{r},\omega) - k_0^2 \epsilon_r(\mathbf{r}) \mathbf{E}(\mathbf{r},\omega) = 0, \tag{1}$$

where $k_0 = \omega/c$ is the wave number in vacuum and ω and c denote angular frequency and speed of the light, respectively. Classically, the electric field from an extrinsic polarization source, $\mathbf{P}_{ex}(\mathbf{r},\omega)$, may be calculated as

$$\mathbf{E}(\mathbf{r},\omega) = \int \mathbf{G}(\mathbf{r},\mathbf{r}',\omega) \frac{k_0^2}{\epsilon_0} \mathbf{P}_{ex}(\mathbf{r}',\omega) \mathrm{d}\mathbf{r}', \tag{2}$$

where the integral is over all space and ϵ_0 is the free space permittivity. $\mathbf{G}(\mathbf{r},\mathbf{r}')$ is the electric field Green's tensor[21,22] which solves the equation

$$\nabla \times \nabla \times \mathbf{G}(\mathbf{r},\mathbf{r}',\omega) - k_0^2 \epsilon_r(\mathbf{r}) \mathbf{G}(\mathbf{r},\mathbf{r}',\omega) = \delta(\mathbf{r}-\mathbf{r}'), \tag{3}$$

subject to the Sommerfeld radiation condition.[23] The interpretation of the Green's tensor becomes clear if we use Eq. (2) to calculate the field from a point source, $\mathbf{P}_{ex}(\mathbf{r},\omega) = \mathbf{d}(\omega)\delta(\mathbf{r}-\mathbf{r}')$, where $\mathbf{d}(\omega)$ is the dipole moment, so that

$$\mathbf{E}(\mathbf{r},\omega) = \mathbf{G}(\mathbf{r},\mathbf{r}',\omega) \frac{k_0^2}{\epsilon_0} \mathbf{d}(\omega), \tag{4}$$

which shows that, in cartesian coordinates, the βth column of the Green's tensor is simply the electric field at $\mathbf{r}$ due to a dipole at $\mathbf{r}'$, oriented along the basis vector $\mathbf{e}_\beta$; namely,

$$\mathbf{E}(\mathbf{r}) \propto \sum_{\alpha=x,y,z} \mathbf{e}_\alpha G_{\alpha\beta} d_\beta, \tag{5}$$

where $d_\beta = \mathbf{d} \cdot \mathbf{e}_\beta$, $\beta \in \{x,y,z\}$.

B. Quantum mechanical description

For a quantum mechanical theory of light emission we start from the multipolar Hamiltonian in the dipole approximation:[20,24]

$$H = \sum_\mu \hbar\omega_\mu a_\mu^\dagger a_\mu + \sum_n \hbar\omega_n b_n^\dagger b_n - i\hbar \sum_{\mu,n} (b_n + b_n^\dagger)(g_{n,\mu} a_\mu - g_{n,\mu}^* a_\mu^\dagger), \tag{6}$$

in which $\hbar$ is the reduced Planck constant and ω_μ, $a_\mu^\dagger$, and a_μ denote angular frequency and creation and annihilation operators, respectively, of a photon in mode μ. The operators satisfy bosonic commutation relations in which

$$[a_\mu, a_\lambda^\dagger] = \delta_{\mu,\lambda}, \tag{7}$$

and all other commutators vanish. Similarly, ω_n, $b_n^\dagger$, and b_n denote angular frequency and creation and annihilation operators, respectively, of an electron-hole pair (an exciton) in the nth QD. These satisfy fermion anticommutation relations where

$$\{b_m, b_n^\dagger\} = \delta_{m,n}, \tag{8}$$

and all other anticommutators vanish. The light-matter coupling strength is given as

$$g_{n,\mu} = \sqrt{\frac{\omega_\mu}{2\hbar\epsilon_0}} \mathbf{d}_n \cdot \mathbf{f}_\mu(\mathbf{r}_n), \tag{9}$$

where $\mathbf{d}_n = d_n \mathbf{e}_n$ denotes the dipole moment of the nth QD of magnitude d_n and orientation $\mathbf{e}_n$. The electromagnetic eigenfunctions $\mathbf{f}_\mu(\mathbf{r})$ are solutions to Eq. (1) and are normalized as

$$\int \epsilon_r(\mathbf{r}) \mathbf{f}_\mu^*(\mathbf{r}) \cdot \mathbf{f}_\lambda(\mathbf{r}) \, \mathrm{d}\mathbf{r} = \delta_{\mu,\lambda}, \tag{10}$$

where the integral is over all space.

Following Refs. 20 and 24, the Heisenberg equations of motion for the photon and exciton creation and annihilation operators can be constructed from the Hamiltonian together with the commutation relations. The equations of motion may be conveniently and elegantly solved in the frequency domain, in which case the electric field is governed by a Lippmann-Schwinger type equation.[25,26] The procedure is clearly explained in Refs. 20 and 24 and we will not repeat it here. We note that the fermionic nature of the excitons complicates the equations of motion in the general case as compared to the harmonic oscillator model used in Ref. 24. However, in the limiting case of a single excitation and in the absence of pure dephasing, the complication vanishes since the projection onto the single excitation subspace renders the equations of motion identical to the harmonic oscillator case.[20] With this approach, the spontaneous emission from excited QDs at the positions $\mathbf{r}_n$ is given in general as the sum of an emitted field and a scattered field as[24]

$$\mathbf{E}(\mathbf{r},\omega) = \sum_n \mathbf{G}^B(\mathbf{r},\mathbf{r}_n,\omega)\mathbf{S}_n(\omega) + \sum_n \mathbf{G}^B(\mathbf{r},\mathbf{r}_n,\omega)\mathbf{U}_n(\omega)\mathbf{E}(\mathbf{r}_n,\omega), \tag{11}$$

where the sum is over all QDs in the sample, and $\mathbf{G}^{\mathrm{B}}(\mathbf{r},\mathbf{r}',\omega)$ denotes the classical background Green's tensor in the absence of QDs. The operator

$$\mathbf{S}_n(\omega) = \mathbf{e}_n \left(\frac{i d_n \omega^2}{\epsilon_0 c^2}\right)\left[\frac{b_n(t=0)}{\omega-\omega_n} + \frac{b_n^{\dagger}(t=0)}{\omega+\omega_n}\right] \quad (12)$$

accounts for the ability of the exciton to act as a source of light and $\mathbf{U}_n(\omega) = \mathbf{e}_n \otimes \mathbf{e}_n U_n(\omega)$ is the scattering potential due to the bare polarizability of the QD in which $\otimes$ denotes the tensor product and

$$U_n(\omega) = \left(\frac{d_n^2\omega^2}{\hbar\epsilon_0 c^2}\right)\left(\frac{2\omega_n}{\omega_n^2-\omega^2}\right). \quad (13)$$

In Ref. 24 it was shown that the electromagnetic propagator that enters Eq. (11) is slightly different from the Green's tensor of classical electromagnetism. The two are different only at $\mathbf{r}=\mathbf{r}'$, however, and only the real part is different. It is well known that the real part of the Green's tensor diverges in this limit and, for this reason, when calculating spontaneous emission in the dipole approximation, a renormalization is usually employed.[24] This renormalization effectively renders the explicit functional form irrelevant for our calculations and we therefore keep the formulation in terms of the classical Green's tensor as defined by Eq. (3). Note that our definition of the Green's tensor differs by a factor of (-1) from the Green's tensor in Ref. 24 and by a factor of k_0^2 from that of Ref. 20. For this reason we have changed the source and the scattering potentials accordingly to keep a consistent notation.

C. Green's tensor calculations

The implicit scattering type formulation of Eq. (11) suggests that we rewrite it in an explicit form as

$$\mathbf{E}(\mathbf{r},\omega) = \sum_n \mathbf{G}^N(\mathbf{r},\mathbf{r}_n,\omega)\mathbf{S}_n(\omega), \quad (14)$$

in which $\mathbf{G}^N(\mathbf{r},\mathbf{r}',\omega)$ contains the scattering properties of all N QDs in the sample and formally is the self-consistent solution to the Dyson equation[26] in the form

$$\mathbf{G}^N(\mathbf{r},\mathbf{r}',\omega) = \mathbf{G}^{\mathrm{B}}(\mathbf{r},\mathbf{r}',\omega) + \sum_n^N \mathbf{G}^{\mathrm{B}}(\mathbf{r},\mathbf{r}_n,\omega)\mathbf{U}_n(\omega)\mathbf{G}^N(\mathbf{r}_n,\mathbf{r}',\omega). \quad (15)$$

Instead of solving Eq. (15) directly, we adopt an iterative approach and write a series of Dyson equations as

$$\mathbf{G}^n(\mathbf{r},\mathbf{r}',\omega) = \mathbf{G}^{n-1}(\mathbf{r},\mathbf{r}',\omega) + \mathbf{G}^{n-1}(\mathbf{r},\mathbf{r}_n,\omega)\mathbf{U}_n(\omega)\mathbf{G}^n(\mathbf{r}_n,\mathbf{r}',\omega), \quad (16)$$

for $1 \leqslant n \leqslant N$ and $\mathbf{G}^0(\mathbf{r},\mathbf{r}',\omega) = \mathbf{G}^{\mathrm{B}}(\mathbf{r},\mathbf{r}',\omega)$. Equation (16) together with the relation $\mathbf{e}_n\mathbf{G}(\mathbf{r}_n,\mathbf{r},\omega) = \mathbf{G}(\mathbf{r},\mathbf{r}_n,\omega)\mathbf{e}_n$ forms the basis of our calculation procedure in which QDs are added to the system one at a time in a self-consistent manner. This is similar to the method that has been developed by Martin *et al.* for the evaluation of the Green's tensor in the coupled dipole approximation.[27] The positions $\mathbf{r}'=\mathbf{r}_n$ are of special importance since the Green's tensor in each of these cases contains also the scattering properties of QD n itself. From Eq. (16), the projection onto the direction $\mathbf{e}_n$ is given as

$$\mathbf{G}^n(\mathbf{r},\mathbf{r}_n,\omega)\mathbf{e}_n = \frac{\mathbf{G}^{n-1}(\mathbf{r},\mathbf{r}_n,\omega)\mathbf{e}_n}{1-\mathbf{e}_n\mathbf{G}^{n-1}(\mathbf{r}_n,\mathbf{r}_n,\omega)\mathbf{e}_n U_n(\omega)}, \quad (17)$$

where the denominator includes the QD self-interaction. The self-interaction inevitably includes a divergent term due to the background Green's tensor $\mathbf{G}^{\mathrm{B}}(\mathbf{r}_n,\mathbf{r}_n)$, which may in principle be removed through a renormalization procedure.[24] For this reason, at $\mathbf{r}=\mathbf{r}'$ we use only the (finite) imaginary part of the background Green's tensor assuming that the effect of the (divergent) real part is already contained in the measured electron mass and transition frequency. Likewise, we will not explicitly include local field effects[28] in the model but assume that the effects are included in the measured dipole moments and transition frequencies of the QDs.

D. Example calculation

As an illustration of the calculation procedure we consider a system with two QDs and drop the explicit ω dependence to ease the notation. Light that is emitted from QD 1 can take one of two routes to the detector; either directly or via scattering off QD 2, as illustrated schematically in Fig. 2. The QD light emission in general is given directly by Eq. (14) with the use of the appropriate Green's tensor. For the two-QD case in Fig. 2, we write the Green's tensor between the QD position $\mathbf{r}_1$ and the position $\mathbf{R} \neq \mathbf{r}_1$ as

$$\mathbf{G}^{(2)}(\mathbf{R},\mathbf{r}_1) = \mathbf{G}^{(1)}(\mathbf{R},\mathbf{r}_1) + \mathbf{G}^{(1)}(\mathbf{R},\mathbf{r}_2)\mathbf{U}_2\mathbf{G}^{(2)}(\mathbf{r}_2,\mathbf{r}_1) \quad (18)$$

$$= \mathbf{G}^{\mathrm{D}}(\mathbf{R},\mathbf{r}_1) + \mathbf{G}^{\mathrm{S}}(\mathbf{R},\mathbf{r}_1), \quad (19)$$

in which, comparing to Fig. 2, we have interpreted the two terms in Eq. (18) as a direct term and a scattering term. It is illustrative to rewrite the total Green's tensor in terms of the background Green's tensors only. Introducing the notation[20]

$$\tilde{\mathbf{G}}^{\mathrm{B}}(\mathbf{r},\mathbf{r}_n) = \frac{\mathbf{G}^{\mathrm{B}}(\mathbf{r},\mathbf{r}_n)}{1-\mathbf{e}_n\mathbf{G}^{\mathrm{B}}(\mathbf{r}_n,\mathbf{r}_n)\mathbf{e}_n U_n} \quad (20)$$

and

$$\tilde{G}_{mn} = \mathbf{e}_m\tilde{\mathbf{G}}^{\mathrm{B}}(\mathbf{r}_m,\mathbf{r}_n)\mathbf{e}_n, \quad (21)$$

we find that the direct term $\mathbf{G}^{\mathrm{D}}(\mathbf{R},\mathbf{r}_1) = \tilde{\mathbf{G}}^{\mathrm{B}}(\mathbf{R},\mathbf{r}_1)$ is simply the Green's tensor in the absence of QD 2. Using Eqs. (16)

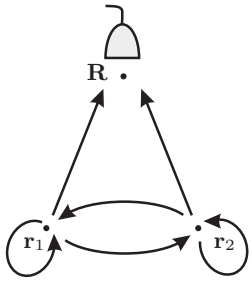

FIG. 2. Schematic of a system with two QDs at the positions $\mathbf{r}_1$ and $\mathbf{r}_2$ and a detector at the position $\mathbf{R}$. Arrows indicate different scattering channels for the light.

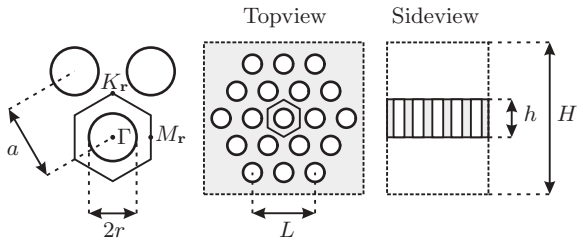

FIG. 3. Sketch of the crystallites. Of special importance are the high-symmetry points in the center and along the edge of the central Wigner-Seitz cell (hexagonal area). In this work we focus on the points $\Gamma = (0,0,0)$, $K_\mathbf{r} = (0,a/\sqrt{3},0)$, and $M_\mathbf{r} = (a/2,0,0)$.

and (17) we may rewrite the projection of the scattering term onto the direction $\mathbf{e}_1$ as

$$\mathbf{G}^{\mathrm{S}}(\mathbf{R},\mathbf{r}_1)\mathbf{e}_1 = \frac{\tilde{\mathbf{G}}^{\mathrm{B}}(\mathbf{R},\mathbf{r}_2)\mathbf{e}_2 U_2 \tilde{G}_{21}}{1-\tilde{G}_{21}U_1\tilde{G}_{12}U_2} + \frac{\tilde{\mathbf{G}}^{\mathrm{B}}(\mathbf{R},\mathbf{r}_1)\mathbf{e}_1 U_1 \tilde{G}_{12}U_2\tilde{G}_{21}}{1-\tilde{G}_{21}U_1\tilde{G}_{12}U_2}, \qquad (22)$$

from which we see that the scattered field itself consists of two terms. One term, $\mathbf{E}_1^{\mathrm{S}}(\mathbf{R})$, corresponds to light that is emitted from QD 1 and scatters off a single QD (QD 2) before arriving at the detector. Another term, $\mathbf{E}_2^{\mathrm{S}}(\mathbf{R})$, corresponds to light that scatters off 2 QDs (first QD 2 and then QD 1) before arriving at the detector.

There is an interesting freedom of choice in the counting of the QDs. In the given example, we could equally well have considered the light emission from QD 2 under the influence of QD 1. In that case the appropriate Green's tensor is given directly in Eq. (17), which we may write as[20]

$$\mathbf{G}^{(2)}(\mathbf{R},\mathbf{r}_2) = \frac{\tilde{\mathbf{G}}^{\mathrm{B}}(\mathbf{R},\mathbf{r}_2) + \tilde{\mathbf{G}}^{\mathrm{B}}(\mathbf{R},\mathbf{r}_1)U_1\tilde{G}_{12}}{1-\tilde{G}_{21}U_1\tilde{G}_{12}U_2}, \qquad (23)$$

corresponding to a direct term and only a single scattering term. The two seemingly different results correspond to different points of view; in Eq. (19) the direct term is independent of the second QD and the second term of Eq. (22) represents a correction due to the second QD. The direct term in Eq. (23), on the other hand, inherently includes the additional dressing due to scattering off QD 2. We emphasize that the Dyson equation procedure in general [and Eq. (18) in particular] is fully consistent with the results of Refs. 20 and 24, but the form is changed to allow for a different interpretation of the terms making up the Green's tensor.

III. PHOTONIC CRYSTALLITE IN DIELECTRIC SLAB

In this section we present calculations of the background Green's tensor for a specific photonic crystal structure. We consider a slab of GaAs ($n = 3.523$) of thickness $h = 150$ nm with a finite-sized triangular PC of air holes with radius $r = 93.3$ nm. The lattice constant is $a = 298$ nm, so that $r/a = 0.313$. The periodic arrangement is terminated to form a small hexagonal crystallite with side length L as illustrated in Fig. 3 for the case of $L = 2a$. The coordinates are chosen so that the middle of the slab is at $z = 0$ and the central air hole is at $(x,y) = (0,0)$.

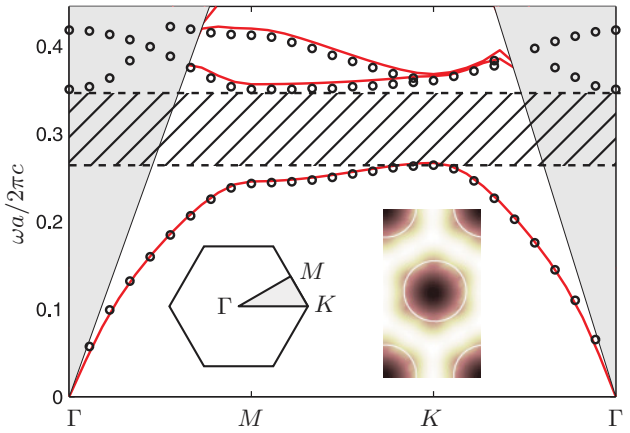

FIG. 4. (Color online) Band diagram for even modes in the infinite PC slab calculated with both the plane wave method (red solid line) and using FDTD (circles). The light cone is indicated by the gray shading and hatching indicates the in-plane band gap. Inset shows the Brillouin zone along with high-symmetry points and the mode profile at the K point.

Figure 4 shows the band structure of the infinite photonic crystal slab calculated using the free plane wave software package MPB, which is based on Ref. 29, as well as the commercial finite-difference time-domain (FDTD) software FDTD SOLUTIONS from Lumerical Inc.[30] For typical applications, such as in Sec. IV, QDs are assumed to be placed in the center of the slab at $z = 0$ to act as sources of single photons. Therefore, the QDs do not couple to odd modes, $\mathbf{E}(-z) = -\mathbf{E}(z)$, and we have included only the even modes, $\mathbf{E}(-z) = \mathbf{E}(z)$, in the band diagram in Fig. 4. The plane wave method is restricted to frequencies below the light line,[31] whereas the FDTD method allows us to track the modes also at frequencies above.

The periodic arrangement of air holes leads to an in-plane band gap, indicated with hatching in Fig. 4, where no light can propagate within the infinite photonic crystal. The modes in the slab are redistributed to frequencies below and above the band gap, and this has profound effects on the radiative coupling between QDs in the PC as described by the Green's tensor. Calculations of the background Green's tensor was carried out using FDTD as described in Ref. 41, and details of the implementation are provided in the Appendix. The vector nature of the electromagnetic field means that visualization of the Green's tensor is difficult, since it consists of nine complex scalars, each of which has a twofold spatial dependence as well as a frequency dependence. We will restrict the analysis to the two positions $K_\mathbf{r}$ and $M_\mathbf{r}$ indicated in Fig. 3 and plot different elements of the tensor as a function of frequency close to the lower band edge. For the remainder of the section we will consider only crystallites with side length $L = 6a$.

The special case of $\mathbf{r} = \mathbf{r}'$ is of particular interest in the context of light emission calculations since the imaginary part of the projected Green's tensor, $\mathbf{e}_\alpha \mathbf{G}(\mathbf{r},\mathbf{r})\mathbf{e}_\alpha$, is proportional to the LDOS. In homogeneous media, with real refractive index n, the projection is independent of orientation and is given as

$$G_0(\omega) = \mathrm{Im}\{\mathbf{e}_\alpha \mathbf{G}^{\mathrm{Hom}}(\mathbf{r},\mathbf{r},\omega)\mathbf{e}_\alpha\} = \frac{n\omega}{6\pi c}. \qquad (24)$$

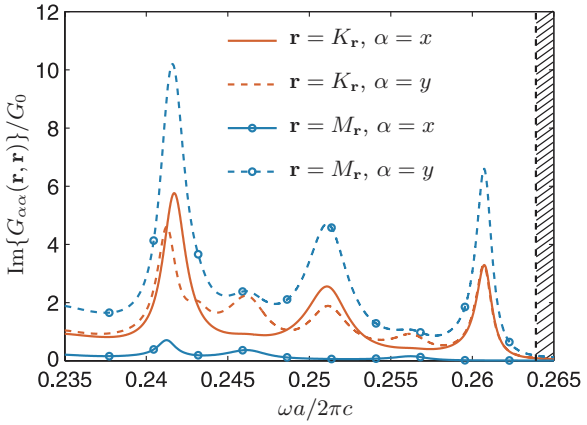

FIG. 5. (Color online) Relative projected LDOS, $\mathrm{Im}\{G_{\alpha\alpha}(\mathbf{r},\mathbf{r})\}/G_0$, for the two positions $K_\mathbf{r}$ and $M_\mathbf{r}$ in a crystallite with side length $L = 6a$. Hatching indicates the in-plane band gap of the infinite crystal.

Figure 5 shows the relative projected LDOS at the two positions of interest. As noted in the introduction, the LDOS is proportional to the decay rate, and the figure therefore directly shows the Purcell effect[7] (i.e., the rate of decay relative to the homogeneous medium). For the $M_\mathbf{r}$ point we observe a quenching of the x-projected LDOS at $\omega a/(2\pi c) \approx 0.26$ and a corresponding increase in the y-projected LDOS. At this frequency, the decay rate at the $M_\mathbf{r}$ point is thus seen to depend sensitively on dipole orientation. At the $K_\mathbf{r}$ point, on the other hand, the decay rate is seen to be independent of orientation at $\omega a/(2\pi c) \approx 0.26$. Light propagation between the two points is described by the Green's tensor $\mathbf{G}(K_\mathbf{r}, M_\mathbf{r}, \omega)$, and in Fig. 6 we show the four elements that are relevant for in-plane oriented electric fields. We notice a pronounced peak of the element G_{xy} and a quenching of the element G_{xx} at $\omega a/(2\pi c) \approx 0.26$. The peaks in the Green's tensor are due to Fabry-Perot-like resonances that shift depending on the size of the crystallite.[32] Using a run-time fast Fourier transform,[33] we may investigate the nature of the resonances by calculating the field at specific frequencies. Figure 7 shows the normalized intensity of the field at $\omega a/(2\pi c) = 0.26$ as excited by an

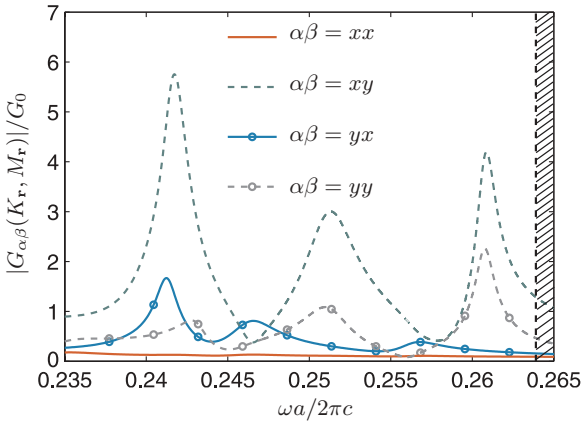

FIG. 6. (Color online) Absolute values, in units of G_0, of elements in the propagator between the points $K_\mathbf{r}$ and $M_\mathbf{r}$ in a crystallite with side length $L = 6a$. Hatching indicates the in-plane band gap of the infinite crystal.

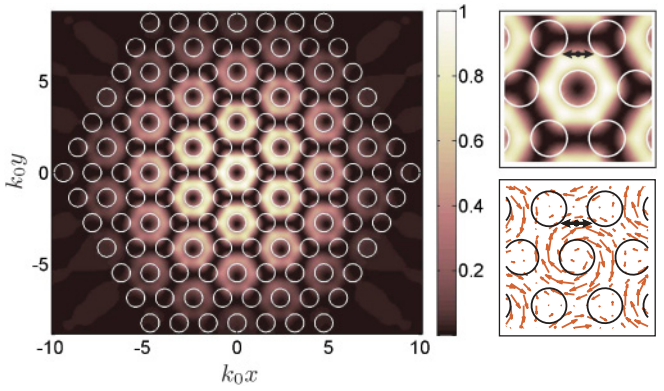

FIG. 7. (Color online) Left: Normalized mode profiles at constant frequency $\omega a/(2\pi c) = 0.26$ as excited by an x-oriented source at the $K_\mathbf{r}$ point. Right: Zoom-in on the central region of the crystallite showing the mode profile (top) and scaled in-plane field vectors (bottom) with a double arrow indicating the source.

x-oriented dipole source at $K_\mathbf{r}$. The calculations were done with an apodization to filter out the contribution from the source at early times, and the fields thus represent the quasi modes of the structure that are initially excited by the source and decay with a finite lifetime given by the width of the peaks in the LDOS. Comparing with the inset of Fig. 4, we see that the field profile displays a periodic structure similar to the Bloch mode at the band edge multiplied by an envelope function to account for scattering at the crystallite edges. This directly illustrates how the crystallite acts as a confinement potential for the Bloch modes. Due to the finite size of the structure, the peak at $\omega a/(2\pi c) \approx 0.26$ does not coincide with the edge of the in-plane band gap from Fig. 4. The position of the peak is expected to converge to the in-plane band edge as the size of the crystal is increased, and we have calculated the LDOS for a number of different sizes of structures, including $L = 18a$, which seems to confirm this assumption. Inspection of the electric field lines of the mode in Fig. 7 reveals that, at this frequency, the field circulates the central air hole. This is the origin of the large value of $G_{xy}(K_\mathbf{r}, M_\mathbf{r})$ as well as the corresponding quenching of $G_{xx}(K_\mathbf{r}, M_\mathbf{r})$ and the x-projected LDOS at the $M_\mathbf{r}$ point.

IV. DECAY DYNAMICS

We now use the numerical calculations of the Green's tensor from Sec. III as a basis for the general Dyson equation approach described in Sec. II. We consider the decay dynamics of two QDs at the positions $\mathbf{r}_1 = K_\mathbf{r}$ and $\mathbf{r}_2 = M_\mathbf{r}$ within a crystallite such as in Fig. 3 with $L = 6a$. The two QDs are assumed to have nearly identical angular frequencies, $\omega_2 = \omega_1 + \Delta\omega$, where $\omega_1 = 1.648 \times 10^{15}$ rad/s is the angular frequency of QD 1 so that $\omega_1 a/(2\pi c) = 0.2607$. In addition, we consider the QDs to have dipole moments of equal magnitude $d_1 = d_2 = 1.00 \times 10^{-28}$ C m, consistent with Ref. 34. Effects of pure dephasing in spontaneous decay from QDs is found experimentally[35,36] to result in energy broadening on the order of μeV. Dephasing tends to dominate the spectra at high temperatures and may be included in the model as an additional broadening of the QD lines.[20] However, in order to highlight the underlying physics

of modified radiative decay, we focus in this work on the low-temperature limit in which radiative decay is the dominant decay mechanism, and we do not include additional dephasing mechanisms in the model.

We will solve for the electric field at the detector position $\mathbf{R} = (0,0,3.3a)$ above the Γ point and outside the membrane (cf. Fig. 1). From Eqs. (12) and (14) it follows that the electric field is made up of positive-frequency parts $\mathbf{E}^+(\mathbf{r},\omega)$ and negative-frequency parts $\mathbf{E}^-(\mathbf{r},\omega)$. From these we can calculate the spectra,[19]

$$S(\mathbf{R},\omega) = \langle [\mathbf{E}^+(\mathbf{R},\omega)]^\dagger \cdot \mathbf{E}^+(\mathbf{R},\omega)\rangle, \tag{25}$$

as well as the corresponding time-domain dynamics. The time-dependent dynamics of the coupled QDs are found from the spectrum by the inverse Fourier transform, and the intensity expectation value is then given as[24]

$$I(\mathbf{R},t) = \langle [\mathbf{E}^+(\mathbf{R},t)]^\dagger \cdot \mathbf{E}^+(\mathbf{R},t)\rangle. \tag{26}$$

The appropriate Green's tensor is given in Eq. (18) and depends on the LDOS at both $K_\mathbf{r}$ and $M_\mathbf{r}$ as well as the propagator between the two positions and the propagators from the QDs to the detector. The propagators out of the crystal $\mathbf{G}(\mathbf{R},\mathbf{r}_{1/2})$ (not shown) do not reflect the resonances of the modes of the photonic crystallite and may be considered constant within the frequency range of Figs. 5 and 6. In addition, the off-diagonal elements of these propagators vanish because of the mirror symmetry of the structure along the x and y axes and the fact that the detector is placed directly above the Γ point. This means that the polarization of the light at the detector position reflects the orientation of the QD dipole moments. At $\omega a/(2\pi c) = 0.2607$, the relevant propagators are listed in Table I. Although the propagators show rich behavior as a function of frequency, they may be considered slowly varying within the bandwidth associated with the decay dynamics. Indeed, a decay time of 1 ns corresponds to an angular frequency linewidth of $\Delta\omega_{\mathrm{BW}} = 10^9$ rad/s (0.7 μeV) which, in the scaled frequencies of Figs. 5 and 6, corresponds to $\Delta\omega_{\mathrm{BW}} a/(2\pi c) = 1.5 \times 10^{-7}$. Therefore, the pole approximation is valid and, in the case of a single QD, this leads to an exponential decay in accordance with the Wigner-Weisskopf theory of spontaneous emission.[37] When a second QD is included, however, the electric field operator

TABLE I. Propagators for the electromagnetic field in the photonic crystallite at $\omega a/(2\pi c) = 0.2607$.

$\mathrm{Im}\{G_{yy}(\mathbf{r}_1,\mathbf{r}_1)\}/G_0$	3.29
$\mathrm{Im}\{G_{xx}(\mathbf{r}_1,\mathbf{r}_1)\}/G_0$	3.29
$\mathrm{Im}\{G_{xx}(\mathbf{r}_2,\mathbf{r}_2)\}/G_0$	0.01
$\mathrm{Im}\{G_{yy}(\mathbf{r}_2,\mathbf{r}_2)\}/G_0$	6.60
$G_{xx}(\mathbf{r}_1,\mathbf{r}_2)/G_0$	$-0.09 + 0.02i$
$G_{xy}(\mathbf{r}_1,\mathbf{r}_2)/G_0$	$0.86 - 3.94i$
$G_{yy}(\mathbf{r}_1,\mathbf{r}_2)/G_0$	$0.29 - 2.23i$
$G_{yy}(\mathbf{R},\mathbf{r}_1)/G_0$	$0.03 + 0.01i$
$G_{xx}(\mathbf{R},\mathbf{r}_2)/G_0$	$0.02 + 0.00i$
$G_{yy}(\mathbf{R},\mathbf{r}_2)/G_0$	$0.05 + 0.02i$

at the position of the detector is given as the sum of a direct term and two scattering terms:

$$\mathbf{E}^+(\mathbf{R}) = \mathbf{E}^{\mathrm{D}}(\mathbf{R}) + \mathbf{E}_1^{\mathrm{S}}(\mathbf{R}) + \mathbf{E}_2^{\mathrm{S}}(\mathbf{R}), \tag{27}$$

corresponding to the different terms in the Green's tensor as discussed in section II D. As we show below, interference between the different terms may lead to pronounced nonexponential decays. Also, the polarization dependence of the propagators may lead to additional nontrivial effects. In order to investigate the role of interference between different terms, and to illustrate the polarization dependence of the propagators, we systematically vary the orientation of the QD dipole moments as well as the initial excitation of the system and obtain very different decay dynamics.

A. QD 1 excited

We consider first the case in which QD 1 is excited at $t = 0$ and decays under the emission of a single photon. The initial condition is thus

$$|\Psi(t=0)\rangle = b_1^\dagger |\mathcal{F}\rangle, \tag{28}$$

where $|\mathcal{F}\rangle$ denotes the Fermi vacuum in which there are no excitations in the semiconductor QDs and $b_n|\mathcal{F}\rangle = 0$.

1. *Both dipole moments in y direction*

Initially, we consider the case where both QDs have dipole moments pointing in the y direction and thus couple through G_{yy}. Figure 8 shows the time-dependent intensities for three different values of the detuning as well as the exponential decay of the single QD. The curves are normalized to the maximum value in the single-QD case. Clearly, an oscillatory behavior is visible in the decay curve for relatively large values of the detuning whereas, for smaller detunings, the oscillations vanish and, generally, the decay is slower than in the single-QD case and show a distinctly nonexponential behavior. Although

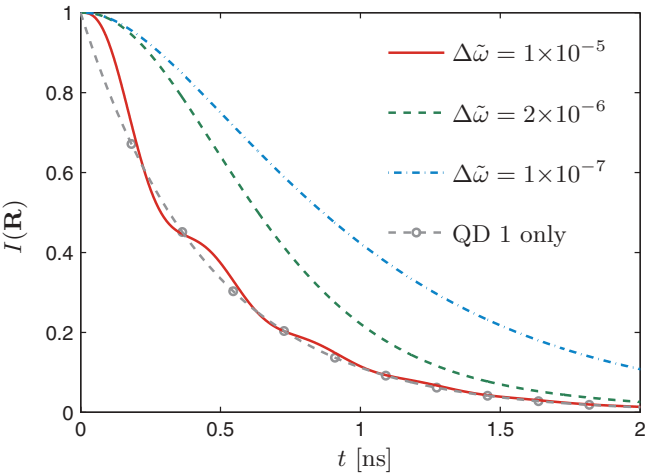

FIG. 8. (Color online) Intensity at the position $\mathbf{R} = (0,0,3.3a)$ of the light emitted from QD 1 at the position $K_\mathbf{r}$ when a second QD with relative detuning $\Delta\tilde{\omega} = \Delta\omega/\omega_1$ is positioned at $M_\mathbf{r}$. Both QDs have dipole moments pointing in the y direction. For reference, we show also the case of a single QD only. The intensity is normalized to the intensity of the single-QD case at $t = 0$.

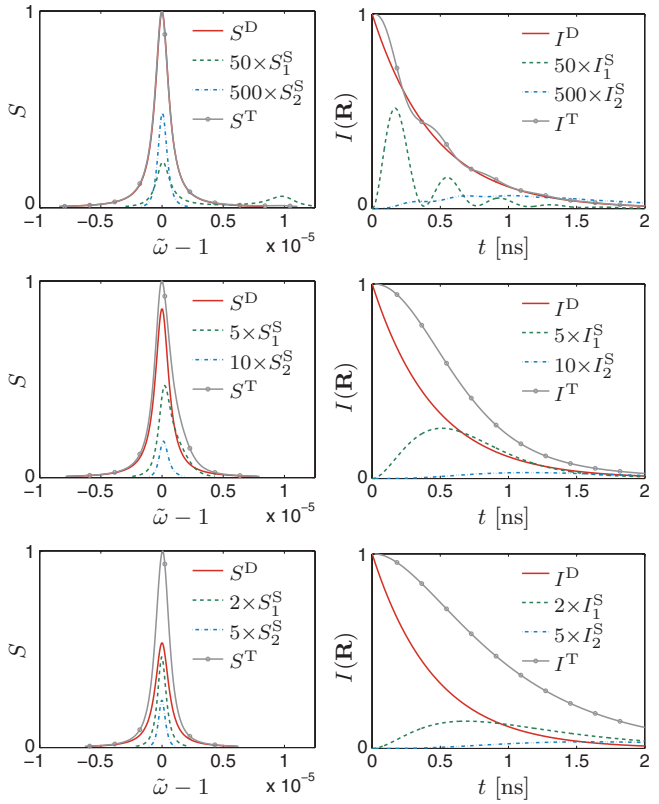

FIG. 9. (Color online) Spectra (left) and decay curves (right) corresponding to the three different decay channels in the two-QD case with QD 1 initially excited. The calculations were performed as in Eqs. (25) and (26) with the electric field given by either the direct term $\mathbf{E}^{\mathrm{D}}$ (red solid lines) or one of the two scattering terms $\mathbf{E}_1^{\mathrm{S}}$ (green dashed line) or $\mathbf{E}_2^{\mathrm{S}}$ (blue dashed-dotted line), as indicated. Gray solid lines show the results as calculated with the total electric fields (equal to the curves in Fig. 8). Results are shown for the three different detunings $\Delta\tilde{\omega} = 10^{-5}$ (top), $\Delta\tilde{\omega} = 2\times10^{-6}$ (center), $\Delta\tilde{\omega} = 10^{-7}$ (bottom), where $\tilde{\omega} = \omega/\omega_1$. The curves corresponding to the scattering channels have been scaled as indicated to make them visible on the scale of the total field.

the detunings are larger than the single-QD linewidth, they are small compared to typical inhomogeneous broadenings on the order of tens of meV (corresponding to $\Delta\tilde{\omega}_{\mathrm{inhom}} \sim 10^{-2}$).

In order to illustrate the effect of the additional terms due to QD 2, we show in Fig. 9, for the three detunings of Fig. 8, the spectra as well as the intensity expectation values for each of the terms individually. Although these separate contributions are not directly observable, this allows a better understanding of the influence of each of the terms responsible for the nontrivial decay dynamics. The spectra and intensities related to the two scattering channels have been scaled in order to make them visible in the figures. For the largest detuning of $\Delta\tilde{\omega} = 10^{-5}$ the splitting of the spectrum is visible as is the corresponding decaying oscillations.

The frequency of the oscillations is determined by the detuning of the QDs as well as the dipole-dipole coupling as mediated by the field in the PC. The latter effect may be dominant in special systems such as high-quality cavities where the emitters couple to long-lived resonances.[38] However, for this material system the lifetime of the PC resonances are vanishingly small compared to the QD lifetimes. Thus, we are in the so-called weak coupling regime, and we interpret the oscillations in the decay curves as arising from interference of the light from the two QDs. For small detunings, the frequency of the oscillations decreases and eventually the time dependence of the term $\mathbf{E}_1^{\mathrm{S}}$ becomes linear in t within the full QD lifetime. Consequently, $I_1^{\mathrm{S}}(\mathbf{R},t)$ increases quadratically at small times until eventually the decaying exponential factor takes over, as seen in Fig. 9. The relatively small detuning is the reason that no oscillations are visible in the I_1^{S} terms for the two smaller detunings. The influence of QD 2 changes qualitatively the decay of QD 1 as measured through the intensity at the detector position. The change in the emission process can be interpreted as the result of absorption and re-emission at QD 2 (for the I_1^{S} term) and at both QD 2 and then at QD 1 (the I_2^{S} term) of the light originally emitted by QD 1. The process is a genuine coherent quantum mechanical phenomenon in which only a single photon is emitted. In particular, the interference at the detector is the interference of the photon with itself.

2. *Orthogonal dipole moments*

We now change the system by rotating the dipole moment of QD 1 to the x direction. In this case, the coupling is mediated by G_{xy} and, since light scatters off both QDs to arrive at the detector (cf. Fig. 2), the light at the detector position has both x- and y-polarized components. To focus on the scattered light from QD 2, we introduce a filter so that only y-polarized light is observed. Figure 10 shows the intensity of y-polarized light at the detector position as a function of time. There is no direct coupling of y-polarized light from QD 1 to the detector and the observed decay is therefore qualitatively different from that of the preceding subsection. Effectively, only the scattering term I_1^{S} is nonvanishing and, comparing to the corresponding term in Fig. 9, we recognize a

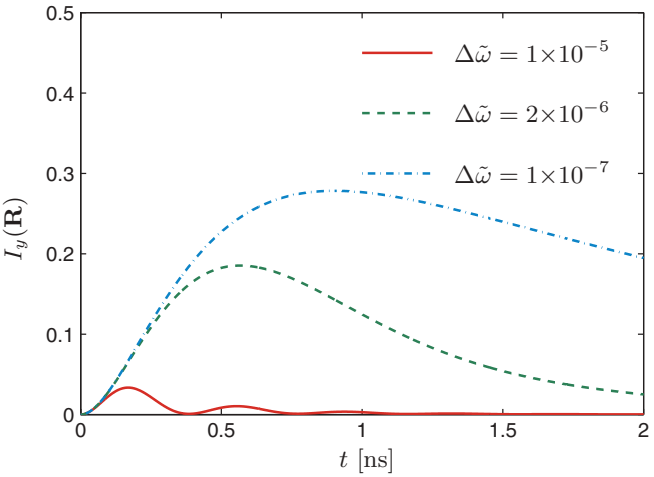

FIG. 10. (Color online) Intensity of y polarized light at the position $\mathbf{R} = (0,0,3.3a)$ emitted from QD 1 at the position $K_{\mathbf{r}}$ with dipole moment in the x direction. The light scatters off a second QD at the position $M_{\mathbf{r}}$ with relative detuning $\Delta\tilde{\omega} = \Delta\omega/\omega_1$ and dipole moment in the y direction. The intensity is normalized as in Fig. 8.

clear similarity, although the scattering term is much larger in this case because the propagator $G_{xy}(K_\mathbf{r}, M_\mathbf{r})$ is larger (cf. Fig. 6).

3. Both dipole moments in x direction

Finally, if we change the system once more by also rotating the dipole moment of QD 2, we see directly from Fig. 6 that the propagator between the two QDs is vanishingly small at the frequency of interest. In this case the scattering of the photon in the PC adds up in a nontrivial way to suppress the coupling between the two QDs, and the decay (not shown) is virtually identical to that of the one-QD case.

B. QD 2 excited

It is illustrative to consider also the case where QD 2 is excited at $t = 0$. We therefore use the initial condition

$$|\Psi(t=0)\rangle = b_2^\dagger|\mathcal{F}\rangle, \tag{29}$$

and we consider the case where both QDs have dipole moments pointing in the y direction. Figure 11 shows the corresponding intensity-decay curves at the detector position. The decay curves are normalized to the maximum intensity of the direct field from QD 1 (as in Fig. 8), and intensities at $t = 0$ is therefore larger than in Fig. 8 because the magnitude of the propagator $\mathbf{G}_{yy}(\mathbf{R}, M_\mathbf{r})$ is larger than $\mathbf{G}_{yy}(\mathbf{R}, K_\mathbf{r})$ (cf. Table I).

Comparing to the decay from QD 1, the dynamics in Fig. 11 are faster, since the LDOS is larger at the $M_\mathbf{r}$ point than at the $K_\mathbf{r}$ point. In addition, the relatively low decay rate of QD 1 means that the scattering terms (not shown explicitly) lead to effects on a slower time scale and hence do not result in the pronounced nonexponential decay at small times observed in Fig. 8.

In typical experiments, the QDs would be excited in an incoherent way and one would monitor the total intensity of the emitted light as a function of time. For a given detuning, the expected decay curve at the detector position

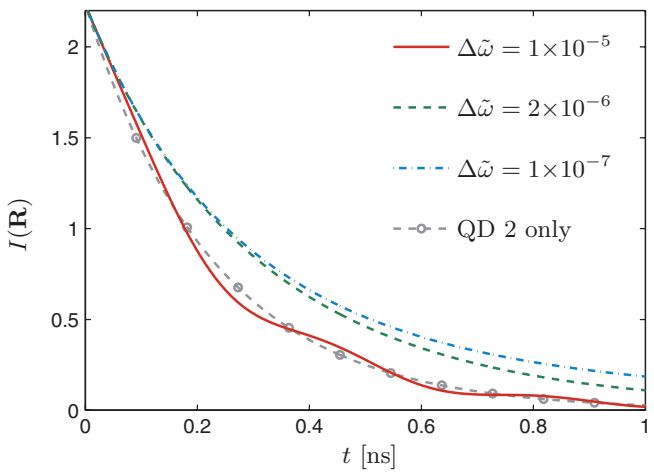

FIG. 11. (Color online) Intensity at the position $\mathbf{R} = (0,0,3.3a)$ of light emitted from QD 2 at the position $M_\mathbf{r}$ with dipole moment in the y direction. The intensity is normalized as in Fig. 8.

TABLE II. Propagators for the electromagnetic field in the homogeneous slab at $\omega a/(2\pi c) = 0.2607$.

$\mathrm{Im}\{G_{yy}(\mathbf{r}_1,\mathbf{r}_1)\}/G_0$	0.86
$\mathrm{Im}\{G_{yy}(\mathbf{r}_2,\mathbf{r}_2)\}/G_0$	0.86
$G_{yy}(\mathbf{r}_1,\mathbf{r}_2)/G_0$	$-0.15 - 0.25i$
$G_{yy}(\mathbf{R},\mathbf{r}_1)/G_0$	$0.02 + 0.01i$
$G_{yy}(\mathbf{R},\mathbf{r}_2)/G_0$	$0.02 + 0.01i$

in this case would be the average of the respective curves in Figs. 8 and 11.

C. Homogeneous slab

For completeness, we consider as a last example the reference system with no photonic crystallite. This consists of a single homogeneous slab of GaAs ($n = 3.523$) of thickness $h = 150$ nm and, as before, we focus on the two positions $\mathbf{r}_1 = K_\mathbf{r}$ and $\mathbf{r}_2 = M_\mathbf{r}$ in the center of the slab at $z = 0$ (cf. Fig. 3). Contrary to the photonic crystallite in Sec. III, the Green's tensor for the homogeneous slab may be expressed in closed form in terms of so-called Sommerfeld integrals.[39] Table II provides the relevant propagators at $\omega a/(2\pi c) = 0.2607$.

Due to symmetry, the LDOS for the homogeneous slab is independent of the in-plane position. Although it does vary with frequency (displaying a characteristic stairway shape similar to the electronic DOS of a quantum well), these variations (not shown) take place on a much larger frequency scale, and we may consider the LDOS constant within the frequency range in Figs. 5 and 6. In particular, the LDOS for the homogeneous slab does not show the characteristic peaks corresponding to the crystallite resonances and, as a consequence, it is somewhat smaller at $\omega a/(2\pi c) = 0.2607$. Comparing the magnitudes of the propagators in Tables I and II, we see clearly the resonance effect of the photonic crystallite acting to confine the light within the structure and thus couple more strongly the two positions.

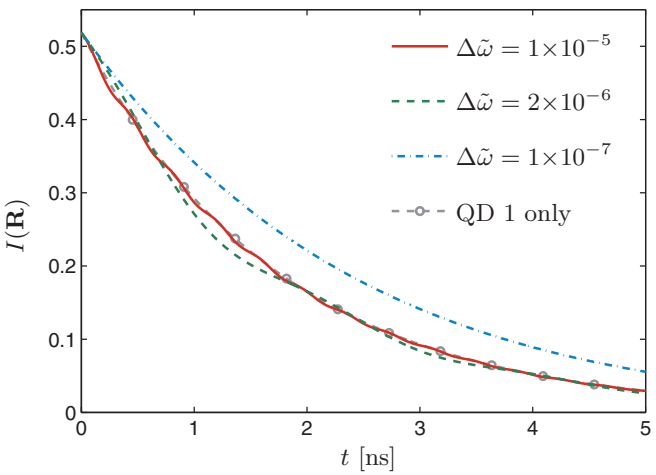

FIG. 12. (Color online) Intensity at the position $\mathbf{R} = (0,0,3.3a)$ of light emitted from QD 1 at the position $K_\mathbf{r}$ within a homogeneous slab of GaAs when a second QD with relative detuning $\Delta\tilde{\omega} = \Delta\omega/\omega_1$ is positioned at $M_\mathbf{r}$. Both QDs have dipole moments pointing in the y direction, and the intensity is normalized as in Fig. 8.

Figure 12 shows the decay dynamics corresponding to the initial condition in Eq. (28) in which QD 1 is initially excited. The decay curves are normalized as in Fig. 8, and therefore the intensities at $t = 0$ are smaller than in Fig. 8, illustrating the redirection effect of the photonic crystallite. In the homogeneous slab, the light can propagate just as easily in-plane as out-of-plane and, therefore, less light ends up at the detector position. Comparing with Figs. 8 and 11, the overall decay is much slower due to the smaller LDOS in the homogeneous slab. Although this provides more time for the scattering terms to build up, the lack of additional scattering from the air holes results in a smaller propagator between the two positions and hence an overall smaller effect from the scattering terms.

V. CONCLUSION

We have investigated decay dynamics of coupled QDs in PC slabs to directly illustrate how QDs, in addition to sources of light, may act as resonant scatterers for light within the crystal. The theoretical method that we have used is based on a self-consistent Dyson equation approach in which QDs are included in the model in a systematic way that is intuitive and physically appealing. The model allows for a direct interpretation in terms of different scattering channels by which a photon may travel from a QD to the detector either directly or by scattering off other QDs. This effect may be interpreted as resonant excitation and subsequent emission at one QD of the photon that was originally emitted from the other QD. It thus represents a highly nontrivial quantum mechanical effect in which the photon interferes with itself.

As an example material system, we have focused on photonic crystallites in dielectric slabs for which an FDTD calculation of the Green's tensor for passive PC slabs (with no QDs) was used as the medium Green's tensor. The detailed scattering properties of the PC as described by the Green's tensor in Figs. 5 and 6 are of key importance in understanding the coupling of the QDs and how it is influenced by position as well as dipole moment orientation. By deliberate coupling of the two QDs through the modes of the PC slab, it was shown how this effect may be exploited to emit light of opposite polarization to that of the emitter or to deliberately inhibit the coupling. For reference, we have also presented calculations based on the Green's tensor for a homogeneous dielectric slab with no crystallite. Although similar decay dynamics are encountered in this case, the lack of additional scattering from the crystallite results in less pronounced effects, as seen directly by comparing Figs. 8 and 12.

The method that we have presented is quite general and is based only on the Green's tensor of the passive background material. We have focused on a single frequency only, corresponding to one of several quasi modes or resonances of the photonic crystallite. In Figs. 5 and 6 one can identify other modes with different field distributions, and these will provide other possibilities for controlling the decay dynamics of embedded QDs emitting at the corresponding frequencies. We have illustrated the method with an example of two scatterers, but the simple form of the Dyson equation approach allows for an easy extension of the method to many scatterers. In addition, the method is not limited to QDs but may equally well be applied to other emitters of light such as nitrogen vacancies in diamond structures.[40] The resonant scattering of light off other QDs in the sample may be important in experiments aiming at measuring properties of single QDs since it could influence the measured light in an uncontrolled way. On the other hand, it offers additional possibilities in terms of light-propagation control that should be of interest for applications.

ACKNOWLEDGMENTS

This work was supported by the Villum Kann Rasmussen foundation via the NATEC center of excellence and the National Sciences and Engineering Research Council of Canada.

APPENDIX: GREEN'S TENSOR CALCULATIONS USING FDTD

In this Appendix, we discuss details concerning the FDTD calculations of the electric field Green's tensor. The approach derives directly from the interpretation of the Green's tensor $\mathbf{G}(\mathbf{r},\mathbf{r}',\omega)$ as the electric field at the position $\mathbf{r}$ due to a point source at the position $\mathbf{r}'$. From Eq. (4) we get an expression for the Green's tensor in the frequency domain. Since FDTD is a time-domain method we apply a transform to arrive at an expression suitable for the FDTD calculations,[41]

$$\mathbf{G}\left(\mathbf{r},\mathbf{r}',\omega\right) = \frac{\epsilon_0 \mathbf{E}(\mathbf{r},\omega)}{k_0^2 \mathbf{d}(\omega)} = \frac{\epsilon_0}{k_0^2} \frac{\mathrm{FT}\left\{\mathbf{E}(\mathbf{r},t)\right\}}{\mathrm{FT}\{\mathbf{d}(t)\}}, \tag{A1}$$

in which FT denotes the Fourier transform and $\mathbf{E}(\mathbf{r},t)$ is the electric field at point $\mathbf{r}$ from the dipole $\mathbf{d}(t)$ located at $\mathbf{r}'$.

In the FDTD simulations, we defined a polarization point source $\mathbf{P}_{\mathrm{ex}}(\mathbf{r},t) = \mathbf{d}(t)\delta(\mathbf{r} - \mathbf{r}_n)$, with time-dependent dipole moment $\mathbf{d}(t)$. We excited the system with a pulse at time t_0 and evolved the system in time, recording at every time step the values of the electric field at predefined detector positions within the calculation domain. The calculation domain was defined as in Fig. 3 with $H = 2100$ nm and perfectly matched layers (PML) as boundaries. The crystallite was fully contained within the calculation domain with a few calculation cells of spacing between the outermost air holes and the boundary. The membrane extended through the PMLs so that the model in effect consisted of an infinite membrane with a single crystallite. An averaging of the refractive index was used for cells along the edge of air holes. We used a Gaussian pulse

$$\mathbf{d}(t) = \mathbf{e}_0 A \exp\left(\frac{-(t-t_0)^2}{2\sigma^2}\right) \sin[\omega_0(t-t_0)], \tag{A2}$$

with an angular frequency $\omega_0 = 1.922 \times 10^{15}$ rad/s and oscillating in the direction $\mathbf{e}_0$. In Eq. (A2), t_0 is the center of the pulse in the time domain and the parameter A ensures that the δ function is properly normalized. For the calculations, we used $\sigma = 3.89 \times 10^{-15}$ s, corresponding to a bandwidth of $\Delta\omega_{\mathrm{BW}} = 2.57 \times 10^{14}$ rad/s (0.17 eV). From Eq. (A1), we expect the numerical Green's tensor to be independent of the exact shape of the pulse as long as the bandwidth is sufficiently large.

[1]Z. Yuan, B. E. Kardynal, R. M. Stevenson, A. J. Shields, C. J. Lobo, K. Cooper, N. S. Beattie, D. A. Ritchie, and M. Pepper, Science **295**, 102 (2002).
[2]J. Claudon, J. Bleuse, N. S. Malik, M. Bazin, P. Jaffrennou, N. Gregersen, C. Sauvan, P. Lalanne, and J.-M. Gérard, Nature Photonics **4**, 174 (2010).
[3]H. J. Kimble, Nature (London) **453**, 1023 (2008).
[4]V. P. Bykov, Sov. J. Quantum Electron. **4**, 861 (1975).
[5]E. Yablonovitch, Phys. Rev. Lett. **58**, 2059 (1987).
[6]S. John, Phys. Rev. Lett. **58**, 2486 (1987).
[7]E. M. Purcell, Phys. Rev. **69**, 681 (1946).
[8]P. Lodahl, A. F. van Driel, I. S. Nikolaev, A. Irman, K. Overgaag, D. Vanmaekelbergh, and W. L. Vos, Nature (London) **430**, 654 (2004).
[9]B. Julsgaard, J. Johansen, S. Stobbe, T. Stolberg-Rohr, T. Sünner, M. Kamp, A. Forchel, and P. Lodahl, Appl. Phys. Lett. **93**, 094102 (2008).
[10]V. S. C. Manga Rao and S. Hughes, Phys. Rev. Lett. **99**, 193901 (2007).
[11]V. S. C. Manga Rao and S. Hughes, Phys. Rev. B **75**, 205437 (2007).
[12]G. Lecamp, P. Lalanne, and J. P. Hugonin, Phys. Rev. Lett. **99**, 023902 (2007).
[13]T. Lund-Hansen, S. Stobbe, B. Julsgaard, H. Thyrrestrup, T. Sünner, M. Kamp, A. Forchel, and P. Lodahl, Phys. Rev. Lett. **101**, 113903 (2008).
[14]R. F. Nabiev, P. Yeh, and J. J. Sanchez-Mondragon, Phys. Rev. A **47**, 3380 (1993).
[15]S. John and T. Quang, Phys. Rev. A **50**, 1764 (1994).
[16]P. Kristensen, A. F. Koenderink, P. Lodahl, B. Tromborg, and J. Mørk, Opt. Lett. **33**, 1557 (2008).
[17]T. Tawara, H. Kamada, Y.-H. Zhang, T. Tanabe, N. I. Cade, D. Ding, S. R. Johnson, H. Gotoh, E. Kuramochi, M. Notomi, and T. Sogawa, Opt. Express **16**, 5199 (2008).
[18]R. Sprik, B. A. van Tiggelen, and A. Lagendijk, Europhys. Lett. **35**, 265 (1996).
[19]S. Hughes and P. Yao, Opt. Express **17**, 3322 (2009).
[20]P. Yao and S. Hughes, Opt. Express **17**, 11505 (2009).
[21]C.-T. Tai, *Dyadic Green Functions in Electromagnetic Theory* (IEEE Press, New York, 1994).
[22]L. Novotny and B. Hecht, *Principles of Nano Optics* (Cambridge University Press, Cambridge, 2006).
[23]P. Martin, *Multiple Scattering. Interaction of Time-harmonic Waves with N Obstacles* (Cambridge University Press, Cambridge, 2006).
[24]M. Wubs, L. G. Suttorp, and A. Lagendijk, Phys. Rev. A **70**, 053823 (2004).
[25]H. Levine and J. Schwinger, Phys. Rev. **74**, 958 (1948).
[26]O. J. F. Martin and N. B. Piller, Phys. Rev. E **58**, 3909 (1998).
[27]O. J. F. Martin, A. Dereux, and C. Gerard, J. Opt. Soc. Am. A **11**, 1073 (1994).
[28]S. Scheel, L. Knöll, and D.-G. Welsch, Phys. Rev. A **60**, 4094 (1999).
[29]S. G. Johnson and J. D. Joannopoulos, Opt. Express **8**, 173 (2001).
[30][http://www.lumerical.com].
[31]S. G. Johnson, S. Fan, P. R. Villeneuve, J. D. Joannopoulos, and L. A. Kolodziejski, Phys. Rev. B **60**, 5751 (1999).
[32]A. F. Koenderink, M. Kafesaki, C. M. Soukoulis, and V. Sandoghdar, J. Opt. Soc. Am. B **23**, 1196 (2006).
[33]S.-H. Kim, S.-K. Kim, and Y.-H. Lee, Phys. Rev. B **73**, 235117 (2006).
[34]J. Johansen, S. Stobbe, I. S. Nikolaev, T. Lund-Hansen, P. T. Kristensen, J. M. Hvam, W. L. Vos, and P. Lodahl, Phys. Rev. B **77**, 073303 (2008).
[35]P. Borri, W. Langbein, S. Schneider, U. Woggon, R. L. Sellin, D. Ouyang, and D. Bimberg, Phys. Rev. Lett. **87**, 157401 (2001).
[36]W. Langbein, P. Borri, U. Woggon, V. Stavarache, D. Reuter, and A. D. Wieck, Phys. Rev. B **70**, 033301 (2004).
[37]V. Weisskopf and E. Wigner, Z. Phys. **63**, 54 (1930).
[38]S. Hughes, Phys. Rev. Lett. **94**, 227402 (2005).
[39]M. Paulus, P. Gay-Balmaz, and O. J. F. Martin, Phys. Rev. E **62**, 5797 (2000).
[40]M. Barth, N. Nüsse, B. Löchel, and O. Benson, Opt. Lett. **34**, 1108 (2009).
[41]P. Yao, V. S. C. Manga Rao, and S. Hughes, Laser and Photonics Reviews **4**, 499 (2010).